Numerical and Theoretical Investigations of Heat Transfer Characteristics in Helium–Xenon Cooled Microreactor Core

Tianshi Wang, Xiang Chai[*], Chaoran Guan, Xinyue Liu, Jiaolong Deng, Hui He, Xiaojing Liu

School of Nuclear Science and Engineering, Shanghai Jiao Tong University, Shanghai 200240, China

[*]Author for correspondence; Email: xiangchai@sjtu.edu.cn (Xiang Chai)

Abstract

Helium–xenon cooled microreactors are a vital technological solution for portable nuclear reactor power sources. To examine the convective heat transfer behavior of helium–xenon gas mixtures in a core environment, numerical simulations are conducted on a cylindrical coolant channel and its surrounding solid regions. Validated numerical methods are used to determine the effect and mechanisms of power and its distribution, inlet temperature and velocity, and outlet pressure on the distribution and change trend of the axial Nusselt number. Furthermore, a theoretical framework that can describe the effect of power variation on the evolution of the thermal boundary layer is employed to formulate an axial distribution correlation for the Nusselt number of the coolant channel, under the assumption of a cosine distribution for the axial power. Based on the simulation results, the correlation coefficients are determined, and a semi-empirical relationship is identified under the corresponding operating conditions. The correlation derived in this study is consistent with the simulations, with an average relative error of 5.3% under the operating conditions. Finally, to improve the accuracy of the predictions near the entrance, a segmented correlation is developed by combining the Kays correlation with the aforementioned correlation. The new correlation reduces the average relative error to 2.9% and maintains satisfactory accuracy throughout the

entire axial range of the channel, thereby demonstrating its applicability to turbulent heat transfer calculations for helium–xenon gas mixtures within the core environment. These findings provide valuable insights into the convective heat transfer behavior of a helium–xenon gas mixture in a core environment.

Nomenclature

A	cross-sectional area of coolant channel (m^2)
a_n	coefficients in Eq. 13
C	constant in Eq. 1
Cp	specific heat at constant pressure (J/(kg·K))
e	constant in Pickett's correlation
F_n	coefficients in series expansion of wall temperature
f	friction factor
G	radial variation of fully developed temperature profile
h	convective heat transfer coefficient (W/(m^2·K))
k	thermal conductivity (W/(m·K))
L	hydraulic diameter of coolant channel (m)
m	mass flow rate (kg/s)
Nu	Nusselt number
ΔNu	10% of average Nu obtained in each run
P	pressure of standard condition (MPa)
Pr	Prandtl number
Pe	Peclet number
Q	power of standard condition (W)
q	heat flux (W/m^2)
Re	Reynolds number
r_0^+	dimensionless coolant channel radius
T	inlet temperature of standard condition (K)
t	temperature (K)
U	velocity of standard condition (m/s)
u	velocity (m/s)
z	axial distance from inlet (m)
$\tilde{z}$	axial distance between end point of integral and inlet (m)

Greek letters

α	constant in Eq. 10
β_n	eigenvalues
γ	distance required downstream of first measuring point to observe a decrease in ΔNu
δ	distance required upstream of last measuring point to observe an increase in ΔNu
ε	eddy diffusivity (m^2/s)
μ	viscosity (Pa·s)
π	circular constant
ρ	density (kg/m^3)
φ	simplified F_n
ω	simplified a_n

Subscripts

avg	average
b	bulk
cor	calculated by correlation
in	inlet
m	momentum
out	outlet
sim	calculated via simulation
t	turbulent
w	wall

1. Introduction

Nuclear microreactors typically generate up to 20 MW_{th} of power and offer numerous advantages, including flexible siting, long operational endurance, high safety level, and high reliability[1]. They can provide power and heat to both industrial facilities and remote communities, and are promising for use in deep-space and deep-sea exploration[2]. To develop microreactors that can generate megawatt-level electrical power, scientists typically employ gas-cooled reactors and the Brayton cycle[3]-[5] to satisfy the requirements of small size, light weight, and simple layout. Furthermore, an appropriate working fluid must be selected to achieve the desired objectives. Incorporating a certain amount of xenon in a helium working fluid can significantly enhance its density and compressibility[6], thus addressing the disadvantages of helium while satisfying the aforementioned requirements. Consequently, gas-cooled reactors with direct cooling and closed helium-xenon Brayton cycles have been investigated extensively for the development of micronuclear power sources.

To satisfy the objectives mentioned above, the molar concentration of xenon in a helium–xenon gas mixture is typically set between 8.6% and 30.0%. Within this range, the Prandtl number (Pr) of the mixture is typically between 0.16 and 0.30[7]. Based on reported data, the Pr range of the helium–xenon gas mixture is lower than that of typical gases such as air, hydrogen, and helium[8] but higher than those of liquid metals such as sodium[9] and lead–bismuth eutectic[10]. This unique Pr range endows the helium–xenon gas mixture with convective heat transfer characteristics that are distinct from those of the aforementioned fluids. Furthermore, in the core flow channel under conditions of high speed, high power, and non-uniform power distribution, the gas properties and structure of the thermal boundary layer undergo significant changes, which consequently affect the convective heat transfer. The preceding discussion clarifies that investigations into the convective heat transfer characteristics of a helium–xenon gas

mixture in an intricate core environment is one of the primary areas of research pertaining to the thermal hydraulics of helium–xenon cooled microreactors.

Numerous significant findings regarding the heat transfer characteristics of helium–xenon gas mixtures have been published. In terms of experiments, Taylor et al.[11] examined the heat transfer properties of mixed gases, including helium–xenon gas mixtures, in a uniformly heated circular tube and assessed the feasibility of several typically used heat transfer correlations. To examine the convective heat transfer characteristics of helium–xenon gas mixtures with various channel geometries, Nakoryakov et al.[12]-[16] investigated the flow and heat transfer properties of a mixture in uniformly heated circular and triangular channels, as well as in circular-triangular transition regions. To achieve the actual geometric structure of a core, Makarov et al.[17] conducted experimental and numerical studies on the heat transfer process of a helium–xenon gas mixture in a thin-walled quasi-triangular pipe, which is suitable for densely packed fuel elements in the core. They analyzed the effects of channel geometry modifications and boundary layer development on the Nusselt number (Nu) and discussed the significant decrease in wall temperature at the exit of the quasi-triangular reign and its underlying causes. In addition, Qin et al.[18] examined the convective heat transfer of helium–xenon gas mixtures in a uniformly heated vertical circular tube. They developed a more accurate Nu correlation and identified an applicable range.

Meanwhile, in terms of simulation, Vitovsky et al.[19] and Lushchik et al. [20] conducted researches on the flow and heat transfer properties of helium–xenon gas mixtures in a uniformly heated small-diameter (5.5 mm) tube. They proposed a method using the mass-average recovery temperature as the characteristic flow temperature, which extended the applicability range of the Dittus–Boelter correlation. In contrast to the approach of Vitovsky et al., Zhou et al. validated the existing turbulent Pr[7] and Nu correlations[21] and proposed new correlations with higher accuracy based on numerical

simulations and theoretical derivations. Additionally, researchers have performed numerical simulations to investigate the heat transfer characteristics of helium–xenon gas mixtures in various channel types, including trilobe channels[22], annular channels, narrow rectangular channels[23], wire-wrapped annular channels[24], and channels with internal vortex generators[25]. Additionally, to simulate the actual operating conditions of a nuclear reactor more accurately, Meng et al.[26] developed a 1/12-scale model of a helium–xenon cooled space reactor core and investigated the effects of bypass vessel cooling, surface radiation, flow channel blockage, and fuel rods on the heat transfer characteristics of the core.

The main objective of most relevant experimental and simulation studies is to establish the Nu correlation, which serves as a critical foundation for the development of multiphysical coupling[27], [28] and system analysis[29], [30] codes for nuclear reactors. However, these studies are based on the fundamental assumption of sufficiently developed temperature and flow fields. Nevertheless, in actual reactors, the power distribution is nonuniform, and the axial power distribution approximates a cosine function[31], [32]. Consequently, the thermal boundary layer inside the channel cannot easily reach a fully developed state[33], thereby affecting the applicability of the Nu correlation in the core channels. To investigate the effect of the thermal boundary layer evolution on heat transfer, Sparrow et al.[34] derived a correlation for the axial Nu distribution of channels under uniform heat flux conditions, including the entrance region. The accuracy of the correlation was verified by comparing it with experimental results. Siegel et al.[35] expanded Sparrow's study and derived a relationship between the variation in the wall-to-bulk fluid temperature difference and the axial position under an arbitrary axial wall heat flux. Based on the studies of Sparrow and Siegel, researchers derived and validated relationships for the axial distribution of Nu under various conditions, including parallel plates[36], laminar flow[37], and a few simple heat

flux distributions[38].

Clearly, investigations into the heat transfer characteristics of helium–xenon gas mixtures under nonuniform power distribution conditions are insufficient. Consequently, studies that investigate the effects of key operational parameters, such as power, flow velocity, and temperature, on the heat transfer characteristics under a nonuniform power distribution are few. Moreover, the applicability of the relevant conclusions in a nonuniform power distribution environment requires further verification.

Regarding the derivation of the Nu correlation, the correlation for the axial Nu distribution is inadequate when the axial power distribution reflects a cosine function and the power density at both the inlet and outlet positions is zero. For microreactors, the volume, mass, and complexity of the system should be reduced by eliminating the axial reflector, thereby resulting in an axial power distribution that conforms to the aforementioned conditions. Furthermore, additional studies are warranted to evaluate the applicability of Sparrow's method to the turbulent heat transfer of low Pr gases in a core environment.

In this study, computational fluid dynamics (CFD) methods are employed to examine the convective heat transfer properties of a helium–xenon gas mixture in a cylindrical coolant channel located within the core of the Small Innovative helium–xenon cooled MObile Nuclear power System (SIMONS)[39]. A three-dimensional multiregion conjugated heat transfer model is developed for one-third of the coolant channel. Based on this model, analyses are performed to investigate the effects of various factors on Nu, including the axial power and distribution, inlet temperature and velocity, and outlet pressure. Subsequently, a theoretical correlation is derived for the axial Nu distribution in the channel, under the assumption of a cosine distribution for the axial power. Using the numerical simulation results, the unknown coefficients in

the correlation are determined and a semi-empirical relationship is developed for the axial Nu distribution. Subsequently, the accuracy of the semi-empirical correlation is tested and compared with those of several existing correlations. Finally, a segmented correlation with higher accuracy is obtained by combining the semi-empirical correlation with another correlation.

2. Model and method

2.1 Geometry model

The SIMONS energy conversion system is based on a closed Brayton cycle, where the core serves as the heat source. The core was designed with a solid structure to achieve system miniaturization. **Figure 1** shows a schematic illustration of the core. The solid core comprised staggered coolant channels and fuel rods. The nuclear fuel used was uranium carbide, the moderator was graphite, and the cladding was composed of a titanium zirconium molybdenum (Mo-TZM) alloy.
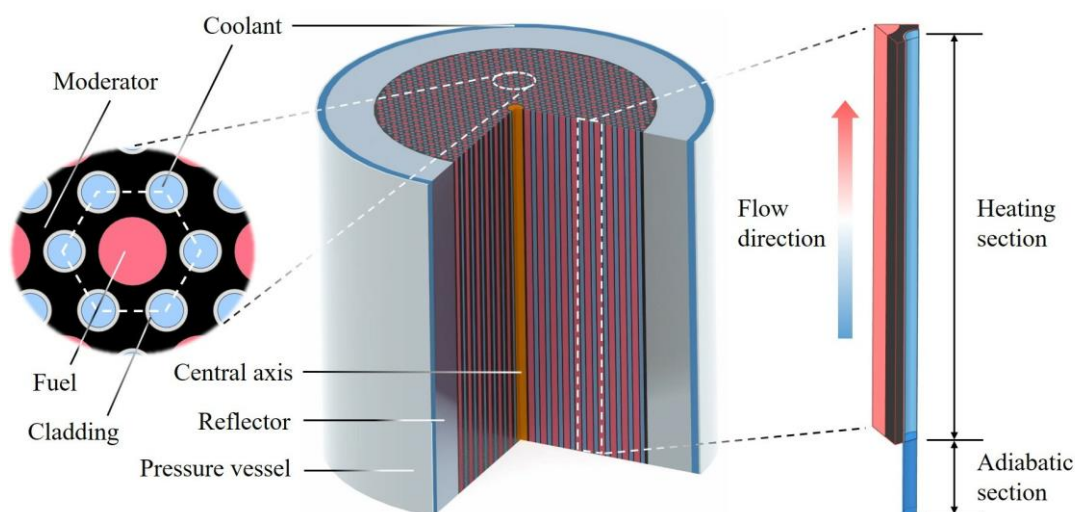

Figure 1. Longitudinal cross-sectional view of the core

In **Figure 1**, the dashed hexagonal line on the left represents a radially repeatable element located in the core. Because this element exhibits radial symmetry, a radial 1/6 structure was utilized for modeling. The details of the constructed geometric model are shown on the right side of **Figure 1**. This model comprised solid regions for the fuel,

moderator, and cladding, whereas the coolant channel was represented by a fluid region.

Under normal operating conditions, the low-temperature helium–xenon gas mixture enters the solid core from the channel inlet at the bottom of the core, is driven by the compressor, absorbs the heat released by the nuclear fuel, and flows out from the outlet at the top of the core. An adiabatic section is incorporated before the inlet to achieve a fully developed flow velocity distribution at the inlet of the heating section. The geometric parameters of the model are listed in **Table 1**.

Table 1. Geometric parameters of the model

Parameter	Value /mm
Diameter of fuel	15.0
Inner diameter of coolant channel	8.0
Thickness of cladding	0.5
Pitch	15.0
Length of coolant channel	1000

2.2 Thermophysical properties

For helium–xenon cooled microreactors that utilize a closed Brayton cycle, the operating pressure of the helium–xenon gas mixture is typically approximately 2 MPa, and the operating temperature is between 400 and 1300 K[21]. To balance the thermal power, efficiency, miniaturization, and lightweight requirements of the system, a helium–xenon gas mixture with a xenon volume fraction of 12% was selected as the working medium for the cycle.

The temperature-dependent properties of the mixture at a pressure of 1.9 MPa are shown in **Figure 2**. Physical properties, such as specific heat, thermal conductivity, and viscosity, are introduced into the CFD software using polynomials that are dependent only on temperature. Density was calculated using the ideal gas equation of state. The physical properties of the solid regions were simplified to constants, as listed in **Table 2**.
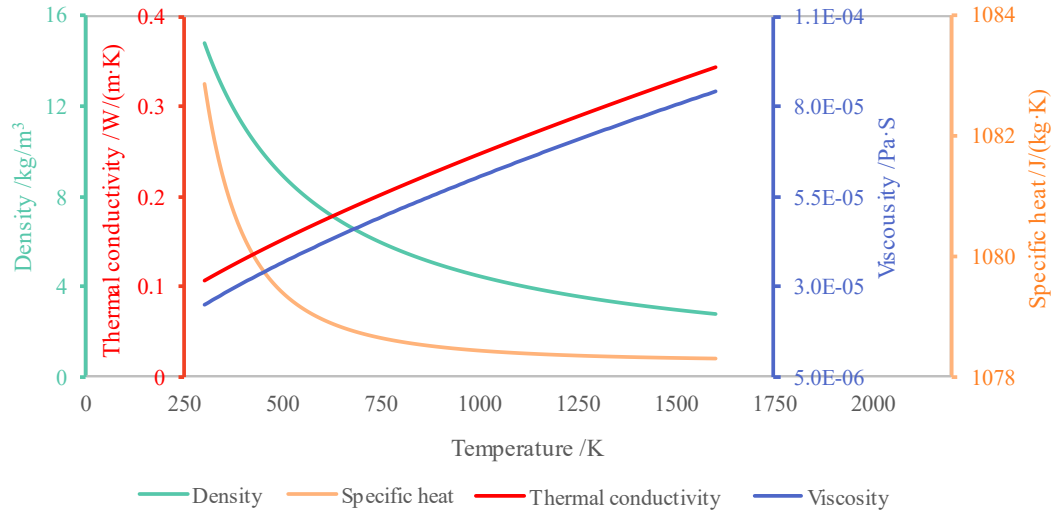
Figure 2. Properties of the helium–xenon gas mixture over the operation temperature

Table 2. Physical properties of materials

Region	Material	Density /kg/m³	Thermal conductivity /W/(m·K)	Specific heat /J/(kg·K)
Fuel	UC	13630.0	25.3	200.0
Moderator	Graphite	1850.0	70.0	1835.0
Cladding	Mo-TZM	10220.0	118.0	255.0

2.3 Numerical models

This study employs the widely utilized CFD software STAR-CCM+ to conduct numerical simulations of flow and heat transfer in nuclear power systems[40], [41]. To balance computational time and resources, the Reynolds-averaged Navier–Stokes method was employed to accommodate turbulence fluctuation terms. A turbulence model was introduced to solve the Navier–Stokes equations. Currently, k-epsilon and shear stress transfer (SST) k-omega models are widely used in high Reynolds number (Re) calculations. The SST k-omega model has been utilized in related studies[21], [22], [42] and yielded satisfactory results; thus, it was employed in this study. To enhance the accuracy and convergence speed, an implicit coupling solver was employed for both the fluid and solid regions.

Pr_t is a dimensionless parameter which affects the turbulent thermal conductivity. As mentioned previously, the helium–xenon mixture used in this study is a low Pr fluid

that possesses properties distinct from those of conventional fluids. A study[7] showed that the Pr_t model developed by Kays[42] can be used to accurately calculate the Pr_t of a helium–xenon gas mixture, as expressed in Eq. 1.

$$Pr_t = \left\{ \frac{1}{2Pr_{t,b}} + CPe_t \sqrt{\frac{1}{Pr_{t,b}}} - (CPe_t)^2 \left[1 - exp\left(-\frac{1}{CPe_t\sqrt{Pr_{t,b}}} \right) \right] \right\}^{-1} \qquad \text{Eq. 1}$$

$$Pe_t = \frac{Pr\ \rho\varepsilon_m}{\mu}, \qquad \text{Eq. 2}$$

where $Pr_{t,b}$ is the Pr_t of the bulk region (0.85), C is a constant (0.3), and Pe_t is the turbulent Peclet number calculated using Eq. 2. Under the conditions investigated, the temperature did not significantly affect Pr.

Using Nu as a metric to quantify the degree of convective heat transfer is a widely recognized practice. Nu is expressed in Eq. 3 as follows:

$$Nu = \frac{Lh}{k}, \qquad \text{Eq. 3}$$

where h is the convection heat transfer coefficient, which is expressed as shown in Eq. 4:

$$h = \frac{q}{t_w - t_b} \qquad \text{Eq. 4}$$

Here, t_b is the bulk temperature, which can be calculated using Eq. 5 as follows:

$$t_b = \frac{\int Cp\rho ut dA}{mCp} \qquad \text{Eq. 5}$$

3. Simulation results

A series of numerical simulations are required to achieve a comprehensive understanding into the flow and heat transfer characteristics of helium–xenon mixtures in the core environment. In the simulation, the channel inlet was modeled as a velocity inlet, whereas the outlet was modeled as a pressure outlet. Additionally, the bottom and top surfaces of the solid region were regarded as adiabatic, and the axial cross-sections of both the fluid and solid regions were assumed to be symmetrical. The fuel region was regarded as a volumetric heat source. In addition, owing to the use of a helium–

xenon gas mixture and metallic cladding, the effects of heat transfer deterioration and power shift resulting from fouling deposition were not considered in the calculations [44], [45].

Nineteen data measurement planes were uniformly distributed along the axial direction of the flow channel. Each measurement plane was positioned at a distance of 0.05 m from one another. No data measurement planes were positioned at the flow channel inlet or outlet. This is because the wall heat flux at these two positions was significantly lower than that at other locations within the channel. Consequently, including these positions in the analysis would yield unrepresentative results and extreme variations in Nu. Such variations are not conducive to subsequent analyses or interpretations.

To investigate the variables that affect convective heat transfer and quantify their respective magnitudes of influence, a sensitivity analysis was performed under five distinct boundary conditions. The operating conditions of the study are presented in **Table 3**, where Run-S was considered as the standard operating condition.

Table 3. Summary of boundary conditions for all operating conditions

Run No.	Power		Inlet		Outlet pressure
	Distribution	Value	Temperature	Velocity	
S	Cosine	Q=3289.5 /W	T=955.0 /K	U=121.9 /m/s	P=1.9 /MPa
D1	Reflector at inlet				
D2	Reflector at outlet				
D3	Reflector at in & outlet	Q	T	U	P
D4	Uniform				
Q1		0.25*Q			
Q2	Cosine	0.50*Q	T	U	P
Q3		0.75*Q			
Q4		1.25*Q			
T1			0.90*T		
T2	Cosine	Q	0.95*T	U	P
T3			1.05*T		
T4			1.10*T		
U1				0.75*U	
U2	Cosine	Q	T	0.88*U	P
U3				1.13*U	

U4				1.25*U	
P1					0.75*P
P2	Cosine	Q	T	U	0.88*P
P3					1.13*P
P4					1.25*P
UQ1		0.73*Q		0.75*U	
UQ2	Cosine	0.88*Q	T	0.88*U	P
UQ3		1.12*Q		1.13*U	
UQ4		1.32*Q		1.25*U	

3.1 Model validation

The model was validated by comparing the simulation and experimental results of Taylor et al. [11]. A schematic diagram of the experimental setup is shown in **Figure 3**; the adiabatic and heating sections of the tube were 328.72 and 352.20 mm long, respectively, and the inner diameter of the tube was 5.87 mm.
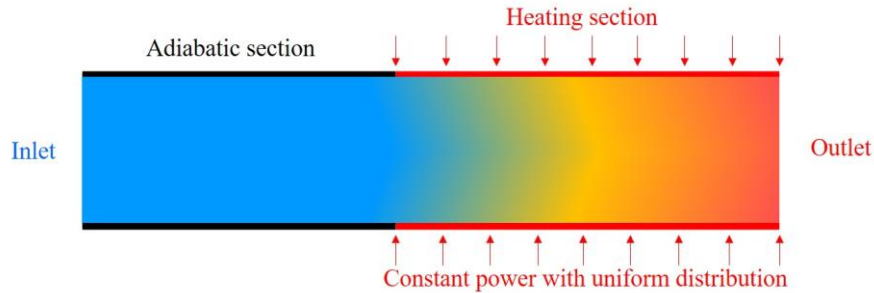
**Figure 3.** Schematic diagram of Taylor's experimental section

To verify the simulation results, data from two runs were selected: Run-689H, which featured gas Pr and Re ranges closest to those in the current study; and Run-715H, which featured gas mole mass and temperature ranges closest to those in the current study. The turbulence model, solver, and Pr_t model used in the simulation were consistent with those described in Section 2. The boundary conditions for the two experiments are listed in **Table 4**, and a comparison of the simulation and experimental results is presented in **Figure 4**.

Table 4. Parameter settings of Taylor's experiments

Run No.	M/g/mol	Pr	Re	T_{in}/K	P_{out}/Pa	Heat flux/W/m^2
689H	83.8	0.25	52350-87373	295.5	481257	96326
715H	14.5	0.30	19485-34042	303.0	807381	296622
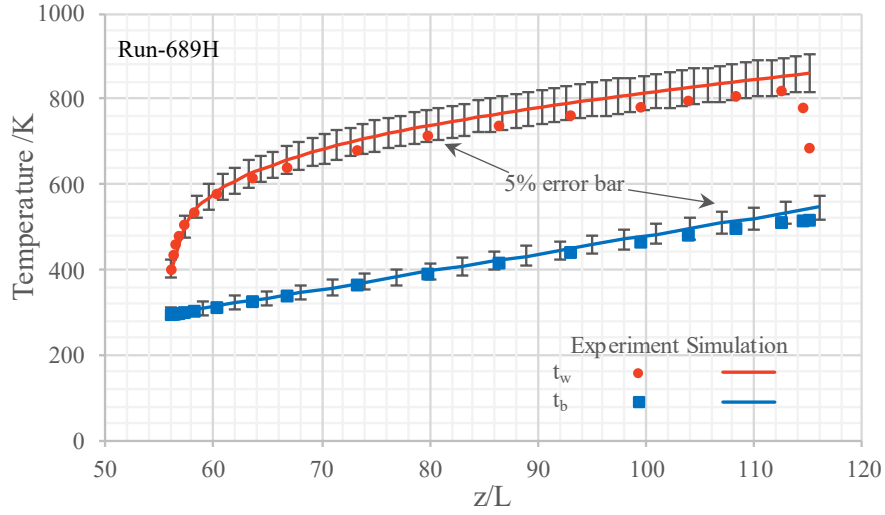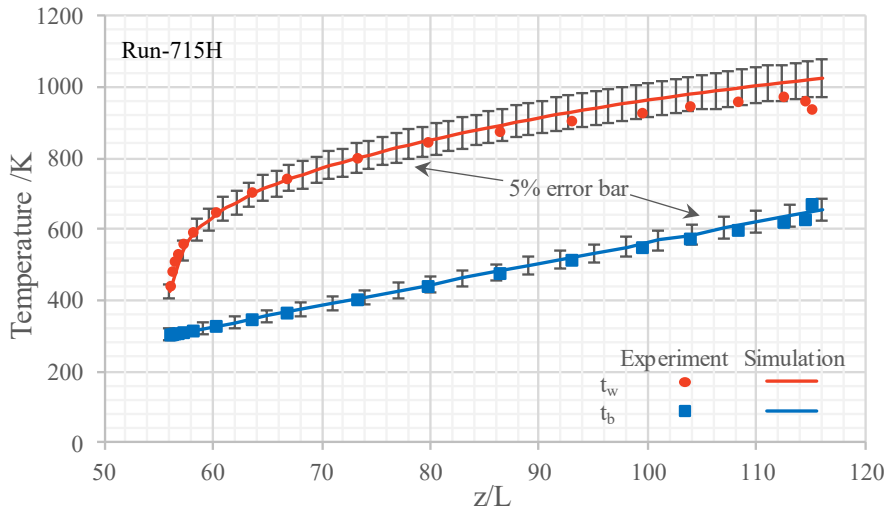
Figure 4. Comparison between simulation and experimental results. (a) Run-689H;
(b) Run-715H.

As shown in **Figure 4**, both experiments showed a significant decrease in the wall temperatures near the outlet, which is likely due to the axial heat conduction of the tube wall[22]. Under two separate operating conditions, the relative error between the experimental and simulated data was less than 5%. The simulated Run-689H and Run-715H exhibited maximum relative errors of 4.4% and 4.2%, respectively, whereas their average relative errors were 2.8% and 1.9%, respectively, except for two points situated near the outlet.

In addition, both the aforementioned model and the core channel model satisfied the criteria for grid independence. **Figure 5** illustrates the grid partitioning of the core

channel model along the axial direction. The grid was refined in the vicinity of the wall within the fluid region to ensure that the center of the first layer of the grid cells was positioned within the viscous sublayer.
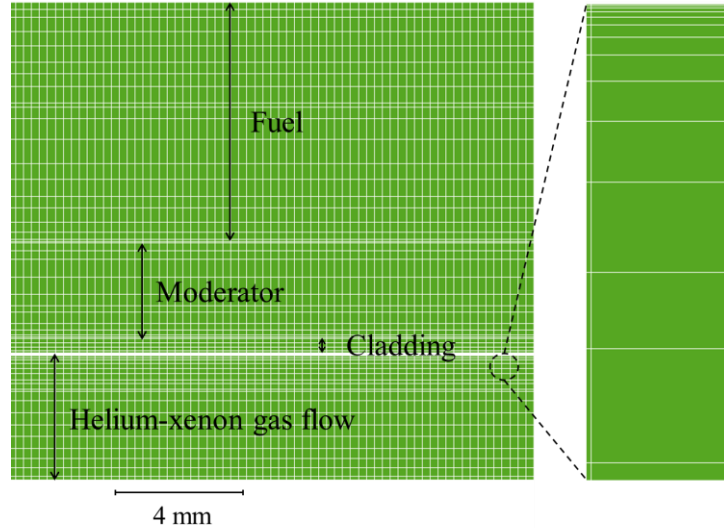

Figure 5. Detailed grid view of the core flow channel model.

3.2 Flow and temperature field of standard condition

To analyze the flow and heat transfer characteristics of the helium–xenon gas mixture in the core environment, one must examine the velocity and temperature distributions in both the flow channel and the surrounding solid region. **Figure 6** shows the radial velocity distribution at various axial positions within the flow channel.

Based on **Figure 6**, the fluid flowed gradually from the inlet to the outlet and the gas expanded owing to the heating of the fuel elements, thus resulting in a velocity increase. Under normal operating conditions, the maximum local velocity in the flow channel reached approximately 199 m/s, which corresponded to approximately 20% of the local speed of sound. Additionally, as shown in **Figure 6**, a significant velocity gradient appeared in the near-wall region. This is attributed to the fluid experiencing resistance from the adjacent wall, which resulted in a lower velocity compared with that at the mainstream flow region.
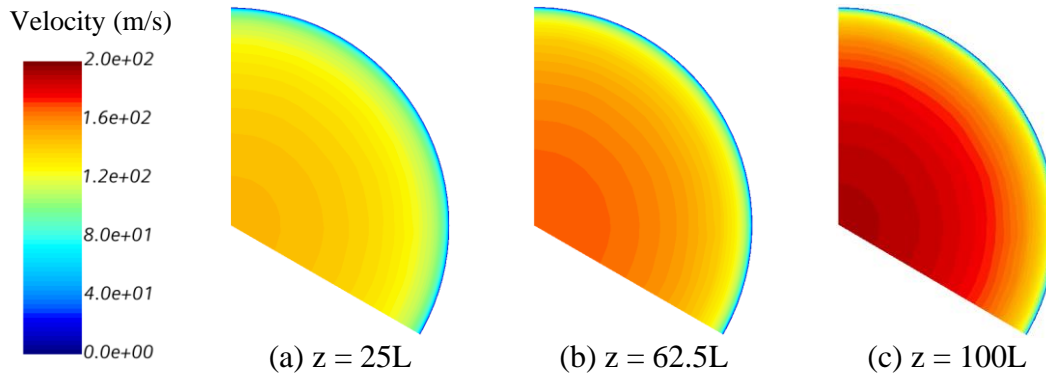
(a) z = 25L   (b) z = 62.5L   (c) z = 100L

Figure 6. Flow velocity distribution at different axial positions.

Figure 7 presents the temperature distribution in both the flow channel and the surrounding solid region. Figures (a)–(c) illustrate the radial temperature distributions at different axial positions, whereas Figure (d) depicts the axial temperature distributions of all four regions.
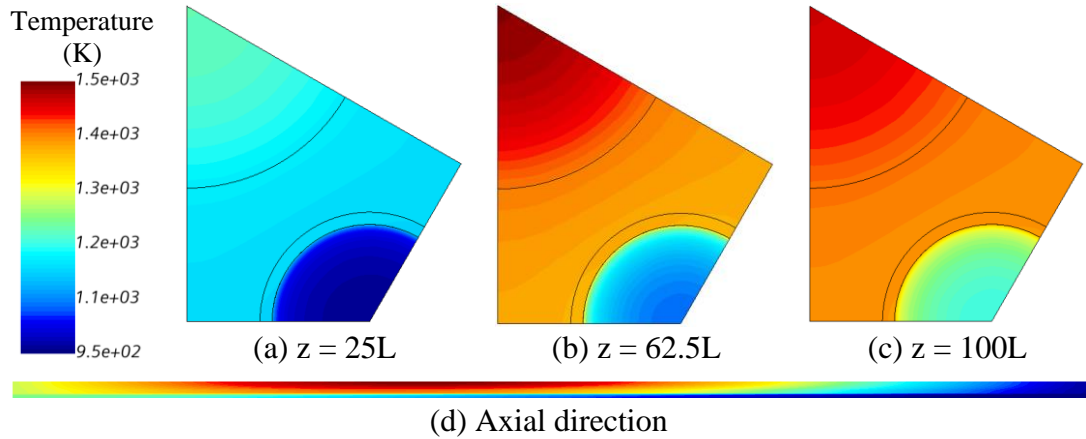

(a) z = 25L   (b) z = 62.5L   (c) z = 100L

(d) Axial direction

Figure 7. Temperature distribution in solid and fluid regions

Based on **Figure 7**, the fuel region demonstrates unsatisfactory thermal uniformity, primarily because of its relatively low thermal conductivity. By contrast, the moderator and cladding regions exhibited better thermal uniformity. Additionally, a significant temperature gradient was observed in the near-wall region of the fluid, where the cladding temperature significantly exceeded that of the helium–xenon gas mixture.

The axial distributions of the radial average temperature for each solid and fluid region is illustrated in **Figure 8**. As shown, the temperature peak points of the three solid regions were located in the latter half of the flow channel. Furthermore, the proximity of a region to the fluid region corresponded to the proximity of its peak temperature point to the outlet. This phenomenon arises because of the gradual increase

in fluid temperature along the flow channel and the cosine distribution of power in the axial direction. Additionally, the helium–xenon gas mixture experienced a rapid temperature increase in the middle of the flow channel and a slower temperature increase at both ends, which is attributable to the cosine distribution of the axial power.
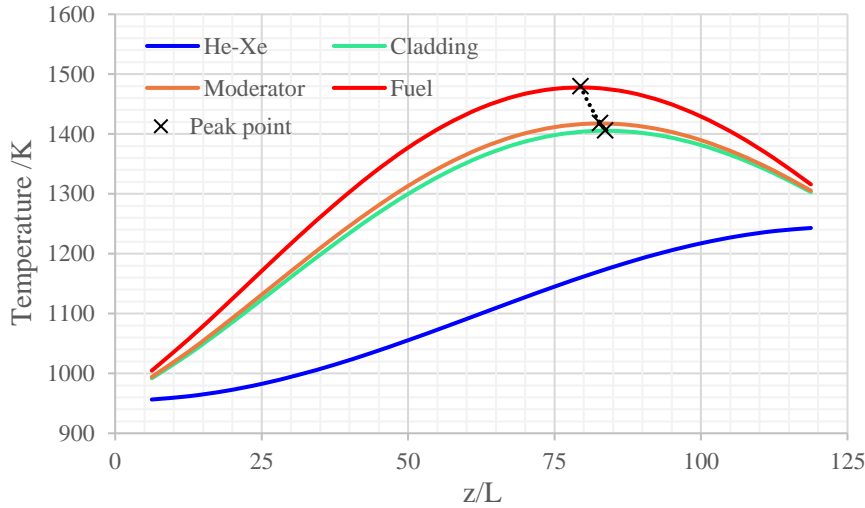

Figure 8. Axial distribution of radial mean temperature in different regions

3.3 Effects of operating parameters on Nu

3.3.1 Power distribution

To render the current study more applicable to practical operating conditions, the axial power distribution for four different operating conditions, namely Run-D1 to Run-D4, was designed based on the actual configuration of the axial reflector in the reactor core and previous heat transfer experiments. **Table 3** presents the boundary conditions for each operating condition and **Figure 9** shows the normalized power distributions.
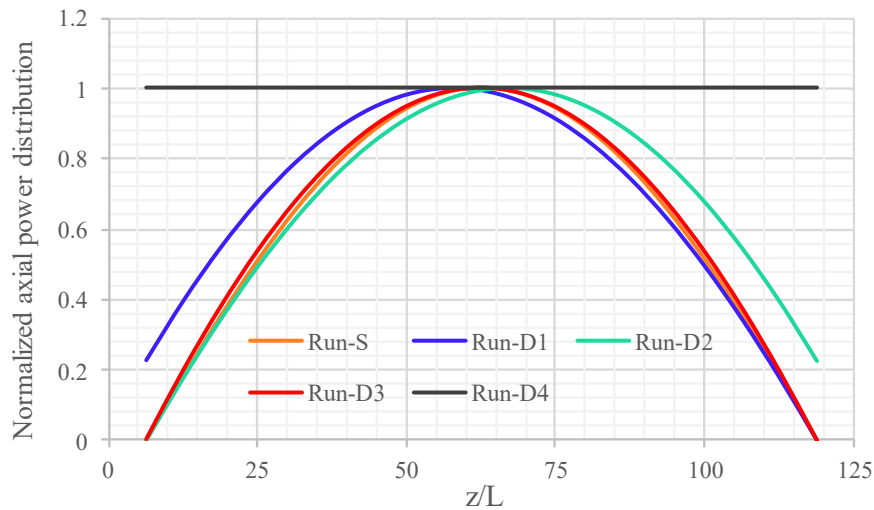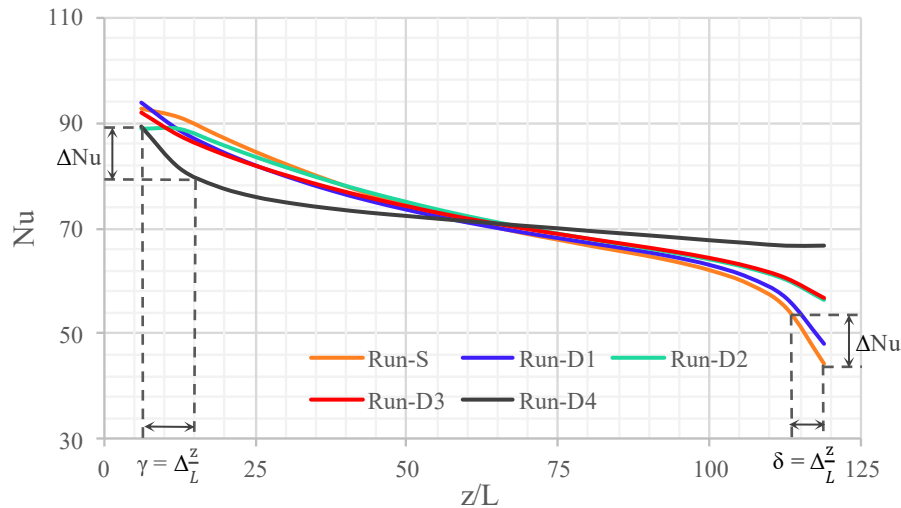
Figure 9. Power distribution under different conditions

Figure 9 shows that the addition of the reflector significantly increased the normalized wall heat flux density near the inlet of Run-D1 and outlet of Run-D2. Additionally, although the normalized wall heat flux distributions for Run-D3 and Run-S were almost identical, the former demonstrated a significantly higher wall heat flux density near the inlet and outlet of the channel than the latter.

Figure 10 shows the axial distribution of Nu under different operating conditions. **Table 5** lists the heat transfer characteristic parameters for each operating condition. To analyze the effects of different factors on the axial change rate of Nu, ΔNu was defined as 10% of the average Nu obtained in each run. Additionally, two dimensionless distances were introduced: γ, which represents the distance required downstream of the first measuring point to observe a decrease of ΔNu, and δ, which represents the distance required upstream of the last measuring point to observe an increase of ΔNu. These values are also marked in **Figure 10**.

Figure 10. Axial Nu distribution under different axial power distributions.

Table 5. Characteristic parameters under different axial power distributions

Run No.	Nu			γ	δ	Unit
	Maximum	Minimum	Average			
S	92.68	44.20	71.73	16.76	4.22	
D1	93.74	48.13	71.59	9.57	5.16	
D2	88.92	56.34	72.96	23.78	17.20	z/L
D3	92.04	56.60	72.62	11.97	17.34	
D4	89.34	66.88	72.59	5.81	82.96	

As shown in **Figure 10**, Nu decreased along the flow direction, and the decreasing trend was consistent across all operating conditions, except for the case of uniform power distribution. In the case of uniform power distribution, Nu decreased significantly near the inlet, whereas the rate of decrease at other positions decelerated considerably. Similar phenomena were reported by Sparrow[34] and Vitovsky[16].

Table 5 indicates that the addition of a reflector at the inlet increased the axial decline rate of Nu near the inlet. By contrast, incorporating a reflector at the outlet can reduce the axial decline rate of Nu, thus improving Nu near the outlet and contributing positively to heat transfer. Hence, incorporating reflectors near the core outlet can potentially provide supplementary thermal safety margins for the core. However, in the case of microreactors, one must scrutinize the tradeoff between the benefits of enhanced thermal safety and the associated increase in core volume and weight resulting from the addition of reflectors.

3.3.2 Power value

To investigate the effect of power on the channel heat transfer, four sets of operating conditions, namely Run-Q1 to Run-Q4, with different power values were designed, and their Nu distributions were compared with those of Run-S. The boundary conditions for each operating condition are listed in **Table 3**. The axial distribution of Nu and the heat transfer characteristic parameters for each operating condition are presented in **Figure 11** and **Table 6**, respectively.
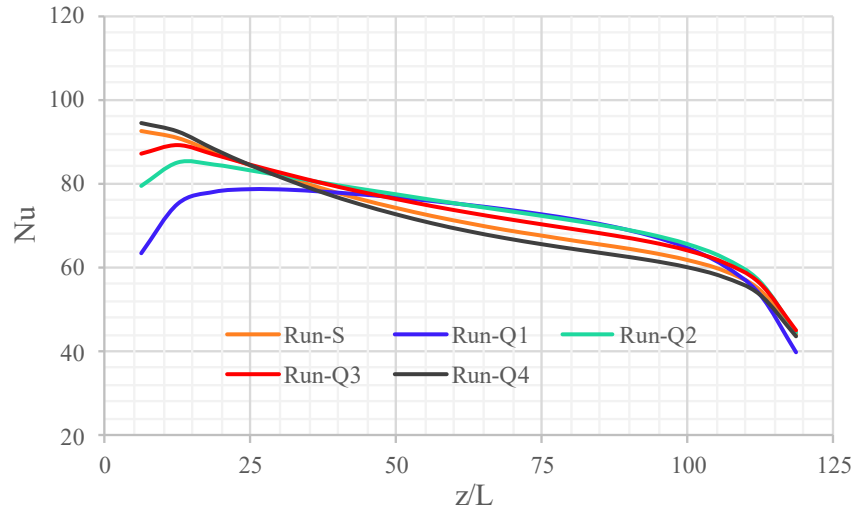
Figure 11. Axial Nu distribution under different power values

Table 6. Characteristic parameters under different power values

Run No.	Nu			δ	Unit
	Maximum	Minimum	Average		
S	92.68	44.20	71.73	4.22	
Q1	78.52	39.97	69.96	3.18	
Q2	85.10	44.34	72.87	3.71	z/L
Q3	89.03	44.96	72.70	4.04	
Q4	94.22	43.60	70.51	4.44	

As shown in **Figure 7**, power exerted a positive effect on Nu near the inlet. However, as the power increased, the effect weakened. Furthermore, the Nu in the axial middle section of the channel decreased gradually as the total power increased. This can be attributed to the lower fluid temperature at lower power levels, which results in a lower viscosity and higher Re under similar flow velocities. Based on the preceding discussion, one can infer that under certain circumstances, such as low-power operation or transient conditions, the phenomenon in which the cladding temperature at the reactor inlet exceeds the expected value must be considered.

In terms of the rate of change of Nu, the distribution of Nu under certain working conditions exhibited a significant nonlinear trend. Hence, only the rate of change of Nu near the outlet is presented in **Table 6**. As shown in the table, the power level did not significant affect the rate of decrease in Nu near the outlet.

3.3.3 Inlet temperature

Operating conditions Run-T1 to Run-T4 were imposed to investigate the effect of the inlet temperature on the axial distribution of Nu. The boundary conditions, axial distribution of Nu, and heat transfer characteristic parameters for each case are presented in **Table 3**, **Figure 12**, and **Table 7**, respectively.
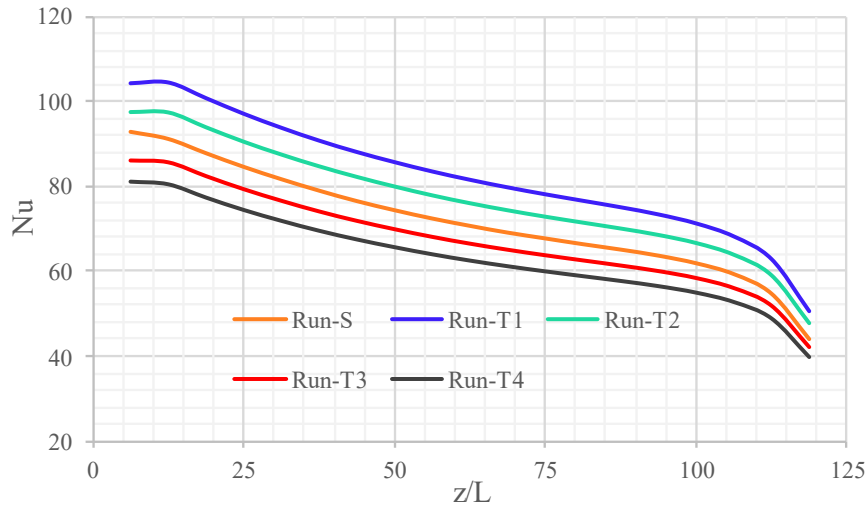

Figure 12. Axial Nu distribution under different inlet temperatures

Table 7. Characteristic parameters under different inlet temperatures

Run No.	Nu			γ	δ	Unit
	Maximum	Minimum	Average			
S	92.68	44.20	71.73	16.76	4.22	
T1	104.67	50.75	82.61	20.79	4.20	
T2	97.48	47.52	76.85	20.13	4.24	z/L
T3	85.90	41.90	67.25	18.68	4.31	
T4	81.01	39.55	63.27	17.99	4.33	

Based on the results presented in **Figure 12** and **Table 7**, as the inlet temperature decreased, the overall Nu in the channel increased, and the rate of increase in the average Nu was approximately -0.094/K. This phenomenon can be attributed to a decrease in the inlet temperature, which resulted to an increase in the fluid density and a decrease in the viscosity, thus causing an increase in Re.

Although reducing the inlet temperature of the core can improve the overall heat transfer efficiency, it may decrease the outlet temperature, which consequently affects the thermal-electric conversion efficiency of the system.

As shown in **Table 7**, the effect of the inlet temperature on the rate of change of Nu near the inlet and outlet was insignificant.

3.3.4 Inlet velocity

The results of the simulations for Runs-U1 to Run-U4 can be used to investigate the effect of the flow velocity on the axial distribution of Nu based on a comparison with the results of Run-S. The boundary conditions, axial distribution of Nu, and heat transfer characteristic parameters for each case are presented in **Table 3**, **Figure 13**, and **Table 8**, respectively.
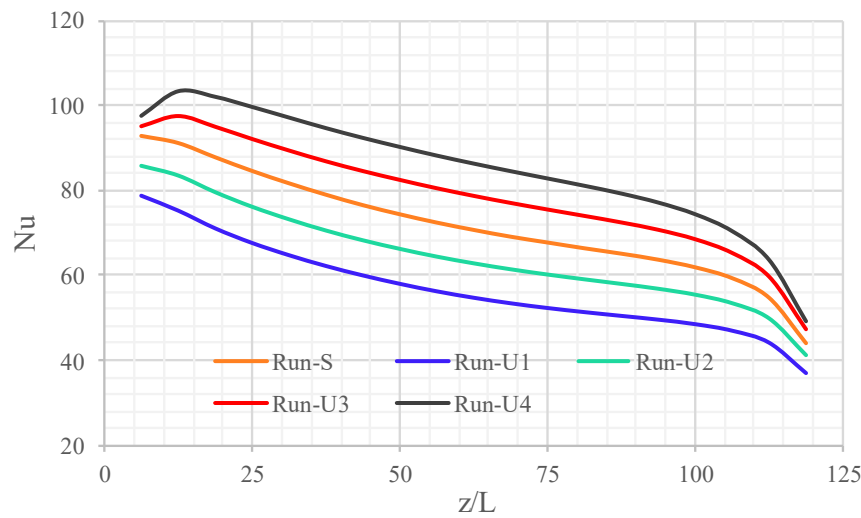

Figure 13. Axial Nu distribution under different inlet velocities

Table 8. Characteristic parameters under different inlet velocities

Run No.	Nu			γ	δ	Unit
	Maximum	Minimum	Average			
S	92.68	44.20	71.73	16.76	4.22	
U1	78.65	36.76	56.80	9.47	4.94	
U2	85.89	40.95	64.46	12.85	4.62	z/L
U3	97.63	47.25	78.62	30.22	3.95	
U4	103.29	49.14	84.89	47.34	3.67	

Based on **Figure 13** and **Table 8**, Nu increased with the flow velocity in the axial middle section of the channel at an average increase rate of 0.468 s/m. This is because an increase in flow velocity improves the mass flow rate and reduces the average fluid temperature, thus resulting in an overall increase in Re.

Furthermore, as the velocity increased, the positive effect of high velocity on Nu

near the inlet weakened gradually, thus resulting in a lower axial decrease rate of Nu near the inlet. Additionally, the effect of the inlet velocity on the axial change rate of Nu near the outlet was insignificant.

Based on the preceding discussion, one can infer that increasing the inlet flow velocity can enhance the overall heat transfer efficiency of the core. However, the rate of improvement in the heat transfer efficiency at the inlet may not be as significant as that in other regions. Consequently, this increase in the flow velocity can result in higher cladding temperatures at the inlet than anticipated.

3.3.5 Outlet pressure

The results of Run-P1 to Run-P4 were compared with those of Run S to investigate the effect of the outlet pressure on the axial distribution of Nu. During the modification of the outlet pressure, the physical properties of the helium–xenon gas mixture were adjusted accordingly. The boundary conditions, axial distribution of Nu, and heat transfer characteristic parameters for each case are presented in **Table 3**, **Figure 14**, and **Table 9**, respectively.
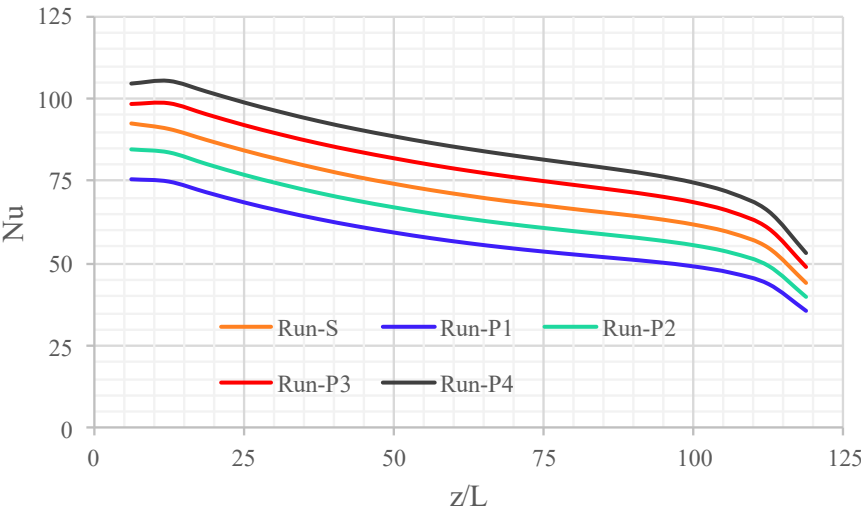

Figure 14. Axial Nu distribution under different outlet pressures

Table 9. Characteristic parameters under different outlet pressures

Run No.	Nu			γ	δ	Unit
	Maximum	Minimum	Average			
S	92.68	44.20	71.73	16.76	4.22	z/L
P1	75.71	35.39	57.50	16.10	4.38	

P2	84.55	39.93	64.81	16.48	4.32
P3	98.32	48.89	78.51	21.99	4.22
P4	105.38	53.03	84.96	24.58	4.18

As shown in **Figure 14** and **Table 9**, Nu increased with the outlet pressure, and the average Nu increased at a rate of approximately 0.031/kPa. The increase in Nu can be attributed to the increase in fluid density caused by the increase in pressure, which results in an overall increase in Re and an improved heat transfer performance.

Caution must be exercised when increasing the inlet pressure to enhance the heat transfer efficiency in the core because it can affect the volume and mass of the compressor, thus potentially affecting the flexibility of the micronuclear reactor power source.

As shown in **Table 9**, the effect of the outlet pressure on the axial change rate of Nu near the inlet and outlet was insignificant.

3.3.6 Inlet velocity under fixed inlet and outlet temperatures

One approach to determine the operating range of a closed Brayton cycle nuclear power system is to vary the core power while maintaining a constant temperature increase in the core and then observe changes in parameters such as the system thermoelectric conversion efficiency. Using this method, operating conditions Run-UQ1 to Run-UQ4 were established by adjusting the total power to maintain a stable outlet temperature based on operating conditions Run-U1 to Run-U4. The simulation results of Run-UQ1 to Run-UQ4 were compared with those of Run-S to evaluate the effects of varying the total power. The boundary conditions, axial distribution of Nu, and heat transfer characteristic parameters for each case are presented in **Table 3**, **Figure 15**, and **Table 10**, respectively.
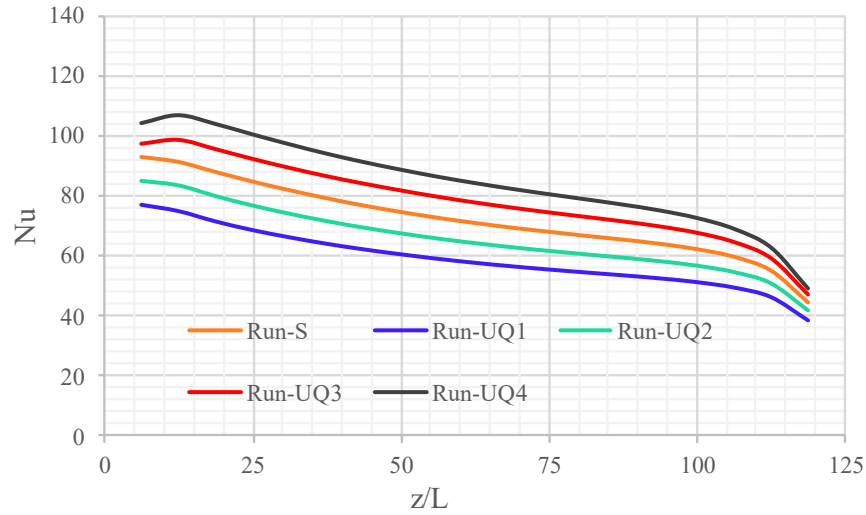
Figure 15. Axial Nu distribution under different inlet velocities with fixed inlet/outlet temperatures

Table 10. Characteristic parameters under different outlet pressures with fixed inlet/outlet temperatures

Run No.	Nu			γ	δ	Unit
	Maximum	Minimum	Average			
S	92.68	44.20	71.73	16.76	4.22	
UQ1	76.70	38.19	58.60	13.20	4.72	
UQ2	84.63	41.49	65.14	15.41	4.52	z/L
UQ3	98.67	47.10	78.25	24.55	4.04	
UQ4	106.78	49.19	84.43	27.86	3.87	

As shown in **Figure 15**, Nu increased with the inlet velocity, and the average Nu increased at a rate of approximately 0.431 s/m, which was lower than the result presented in Section 3.3.4.

As shown in **Table 10**, similar to the conclusion in Section 3.3.4, as the inlet velocity increased, the positive effect of the high velocity on Nu near the inlet gradually weakened. However, under the operating conditions investigated in this section, this weakening trend became less pronounced owing to the change in the power. Furthermore, the inlet velocity did not significantly affect the decreasing rate of Nu near the outlet.

4. Correlation for axial Nu distribution

4.1 Theoretical derivation

To depict the axial variation in Nu in the channel in the core environment precisely, a theoretical framework that can capture the changing behavior of the thermal boundary layer is necessary. Sparrow et al. presented a theoretical derivation based on the theory of turbulent boundary layers and eddy viscosity. According to their theory, the wall-to-bulk temperature difference along the axial direction of a circuit channel under turbulent heat transfer conditions of forced convection with a uniform axial power distribution can be expressed as shown in Eq. 6[34].

$$t_w - t_b = \frac{qL}{2k}\left\{G(r_0^+) + \sum_{n=0}^{\infty} F_n \, exp\left[-\frac{4\beta_n^2}{Re}\frac{z}{L}\right]\right\}, \qquad \text{Eq. 6}$$

where $G(r_0^+)$ denotes the dimensionless wall-to-bulk temperature difference in the fully developed temperature field; F_n is the coefficient of the series expansion of the wall temperature, which is a negative value that depends only on Re, Pr, and G; β_n^2 is the eigenvalue and is related only to Re and Pr. The derivation of Eq. 6 is based on the following six assumptions:

I. The fluid properties are constant.

II. Compared with the radial heat diffusion, the axial diffusion of both molecular and turbulent heat is negligible.

III. The mean value of the radial velocity is 0.

IV. Viscous dissipation is negligible.

V. The turbulence velocity distribution is fully developed throughout the channel.

VI. The turbulent Pr can be approximated as 1.

This equation can be used to precisely calculate the distribution of the axial wall-to-bulk temperature difference, including that at the thermal entrance region. Additionally, $G(r_0^+)$ can be expressed as

$$G(r_0^+) = -\sum_{n=0}^{\infty} F_n \qquad \text{Eq. 7}$$

Based on Eq. 6, when z = 0 (i.e., at the entrance), the wall-to-bulk temperature

difference is 0; when z = ∞ (i.e., where the temperature is fully developed), the temperature difference is a constant.

For operational conditions with an arbitrary axial power distribution, the power distribution can be regarded as a combination of multiple power steps, with each power step affecting the downstream temperature distribution[35]. Based on Eq. 6, if no heat flux appears on the wall before position z and a uniform heat flux of dq appears after z, then the temperature difference downstream $\tilde{z}$ can be calculated as

$$t_w - t_b|_{\tilde{z}} = dq \cdot \frac{L}{2k} \left\{ G(r_0^+) + \sum_{n=0}^{\infty} F_n \, exp\left[-\frac{4\beta_n^2}{Re} \frac{\tilde{z}-z}{L} \right] \right\} \quad (z \le \tilde{z}) \qquad \text{Eq. 8}$$

Integrating the equation above yields the following expression for the wall-to-bulk temperature difference at $\tilde{z}$ under an arbitrary axial power distribution[35]:

$$t_w - t_b|_{\tilde{z}} = -\frac{2}{kRe} \sum_{n=0}^{\infty} F_n \beta_n^2 \int_0^{\tilde{z}} q(z) \exp\left[-\frac{4\beta_n^2}{Re} \frac{\tilde{z}-z}{L} \right] dz \qquad \text{Eq. 9}$$

Without axial reflectors, the axial power distribution in the core can be approximated using a cosine function as follows:

$$q(z) = \alpha cos\left[\pi(z - \frac{1}{2}) \right] \qquad \text{Eq. 10}$$

After simplification, it can be expressed as

$$q(z) = \alpha sin\,(\pi z) \qquad \text{Eq. 11}$$

By substituting Eq. 11 into Eq. 9, the equation for the wall-to-bulk temperature difference at $\tilde{z}$ under a cosine power distribution can be obtained as follows:

$$t_w - t_b|_{\tilde{z}} = -\frac{2\alpha}{kRe} \sum_{n=0}^{\infty} F_n \beta_n^2 \frac{\int_0^{\tilde{z}} sin\,(\pi z) exp\left[\frac{4\beta_n^2}{Re} \frac{z}{L} \right] dz}{exp\left[\frac{4\beta_n^2}{Re} \frac{\tilde{z}}{L} \right]} \qquad \text{Eq. 12}$$

Let $a_n = \frac{4\beta_n^2}{ReL}$. Therefore, the temperature difference at $\tilde{z}$ can be expressed as

$$t_w - t_b|_{\tilde{z}} = \frac{2\alpha}{kRe} \sum_{n=0}^{\infty} F_n \beta_n^2 \frac{\pi cos\,(\pi\tilde{z}) - \frac{\pi}{exp(a_n\tilde{z})} - a_n sin\,(\pi\tilde{z})}{a_n^2 + \pi^2} \qquad \text{Eq. 13}$$

The axial distribution of Nu[-1] under the cosine power distribution is represented as shown in Eq. 14.

$$Nu^{-1} = \frac{t_w - t_b}{q(\tilde{z})}\frac{k}{L}$$

$$= \frac{1}{2}\sum_{n=0}^{\infty}\frac{F_n a_n}{a_n^2 + \pi^2}\left\{\pi\left[cot\,(\pi\tilde{z}) - \frac{1}{sin\,(\pi\tilde{z})exp\,(a_n\tilde{z})}\right] - a_n\right\} \qquad \text{Eq. 14}$$

In Eq. 14, when $\tilde{z}$ approaches 1 m from the left side, the following equation is satisfied.

$$\lim_{\tilde{z}\to 1^-}\left\{\pi\left[cot\,(\pi\tilde{z}) - \frac{1}{sin\,(\pi\tilde{z})exp\,(a_n\tilde{z})}\right] - a_n\right\} = -\infty \qquad \text{Eq. 15}$$

Thus, in the region near the channel outlet, Nu^{-1} approaches infinity, whereas Nu approaches zero ($a_n > 0$, $F_n < 0$). As $\tilde{z}$ approaches 0 m from the right side, it satisfies the following equation:

$$\lim_{\tilde{z}\to 0^+}\left\{\pi\left[cot\,(\pi\tilde{z}) - \frac{1}{sin\,(\pi\tilde{z})exp\,(a_n\tilde{z})}\right] - a_n\right\} = 0 \qquad \text{Eq. 16}$$

Hence, near the inlet, Nu^{-1} approaches 0, whereas Nu approaches infinity.

As shown in Eq. 14, F_n and a_n are critical parameters that affect the Nu. In Sparrow and Siegel's series of studies[34], [35], the values of F_n and a_n were obtained by solving the eigenvalue system of the Sturm–Liouville type, which is based on the six assumptions mentioned above. In this study, the high flow velocity of the helium–xenon gas mixture renders viscous dissipation a significant factor that affects the Nu distribution under certain operating conditions. Moreover, the gas is heated vigorously in the channel, thus causing changes in the physical properties and a pronounced acceleration effect. This renders it challenging to satisfy the conditions of constant properties and a fully developed turbulent velocity distribution. Therefore, the six assumptions mentioned earlier may not be entirely valid, whereas solving the eigenvalue equation to determine F_n and a_n may introduce a significant deviation.

In addition, coefficients F_n and a_n in Eq. 14 are related to the characteristic values, which result in an infinite number of unknown coefficients that must be determined, thereby rendering the equation impractical for engineering applications. To reduce the number of unknown coefficients, F_n and a_n in Eq. 14 were simplified as φ and ω, respectively, and existing simulation data were used to determine the values of φ and ω for various operating conditions. The subsequent analysis indicates that this

simplification affected the accuracy of the relationship at a reasonable level. Hence, Eq. 14 can be simplified as follows:

$$Nu = 2\frac{\omega^2 + \pi^2}{\varphi\omega}\left\{\pi\left[\cot(\pi\tilde{z}) - \frac{1}{\sin(\pi\tilde{z})\exp(\omega\tilde{z})}\right] - \omega\right\}^{-1} \qquad \text{Eq. 17}$$

Using the MATLAB Genetic Algorithm Toolbox, the axial distribution of Nu for all operating conditions in Section 3, which presents axial power distributions in the form of a cosine function (excluding Run-Q1 and Run-Q2, which exhibited clear nonlinear trends), was fitted using Eq. 17. The variations in -φ and ω with the average Re of each operating condition are presented in **Figure 16**. The average Re of each condition was calculated as follows:

$$Re_{avg} = \frac{Re_{in} + Re_{out}}{2} = \frac{2m(\mu_{in} + \mu_{out})}{\pi L \mu_{in}\mu_{out}} \qquad \text{Eq. 18}$$

(a) -φ

(b) ω
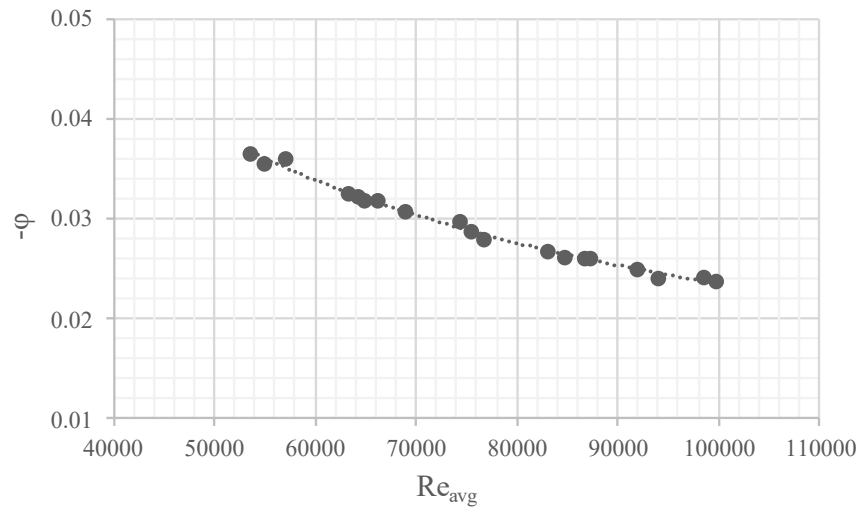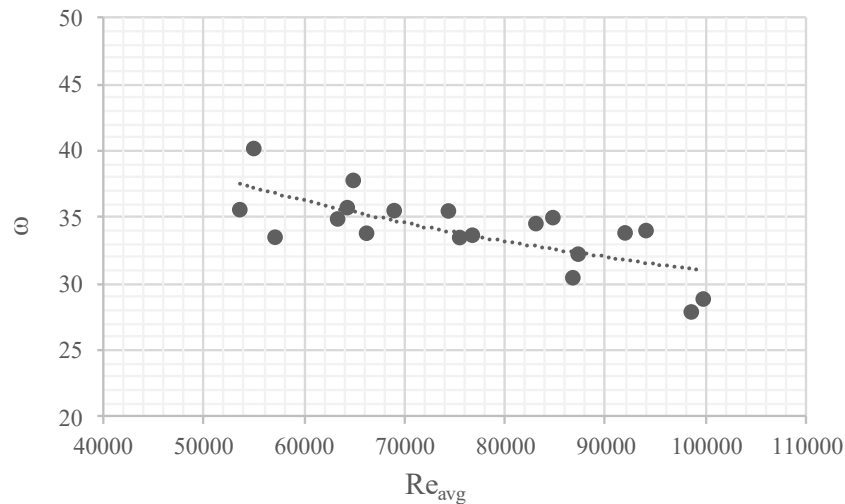
Figure 16. Relationship between the coefficients and average Re (dashed line represents the function graph of the fitted equation, and the average Re is within the range of 5.3×10^4 to 1×10^5)

When Pr = 0.264 and the average Re was between 5.3×10^4 to 1×10^5, the relationship between φ and the average Re, as well as that between ω and the average Re, were fitted using power functions. The results are expressed as shown in Eqs. 19 and 20.

$$\varphi = -90.72 Re_{avg}^{-0.72} \qquad \text{Eq. 19}$$
$$\omega = 1075.65 Re_{avg}^{-0.31} \qquad \text{Eq. 20}$$

Here, the Nu at any axial position $\tilde{z}$ in the flow channel can be calculated conveniently using Eq. 17 . In the following section, $\tilde{z}$ is uniformly substituted with z in the relevant correlations to facilitate understanding.

4.2 Verification and analysis

As shown in **Figure 17**, the axial Nu distribution calculated using Eq. 17 was compared with the simulation results for all the operating conditions listed in **Table 3**, where the axial power distribution was cosine (excluding Run-Q1 and Run-Q2).
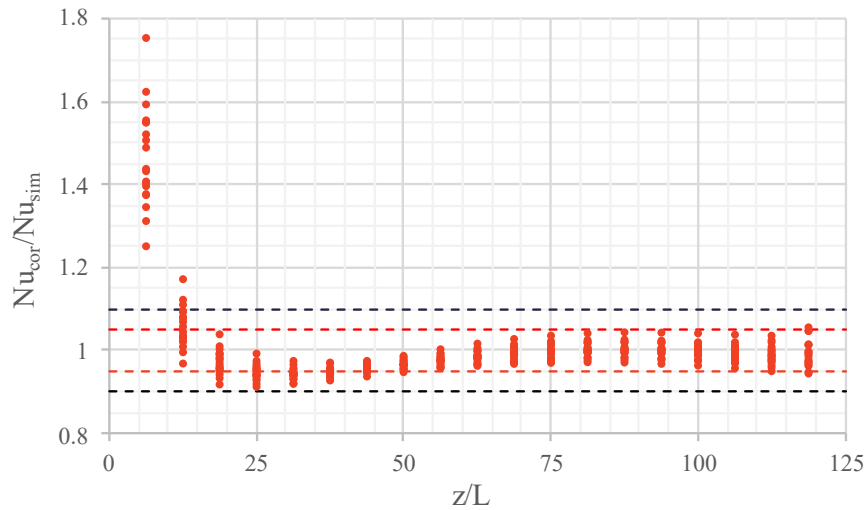

Figure 17. Comparison of calculations using Eq. 17 with simulation results (relative error within red and black dashed lines is less than 5% and 10%, respectively)

As shown in **Figure 17**, the most significant difference was indicated in the region near the inlet, with a maximum relative error of 75.3%, whereas the average relative error was approximately 5.2%. Approximately 94% of the data points showed a relative

error within 10%, of which and 78% indicated a relative error within 5%. Moreover, in the latter half of the channel (z/L ⩾ 62.5), almost all the data points showed a relative error within 5%.

Table 11 presents the boundary conditions of the four newly established cases, which are distinct from those in Table 3, used to assess the validity of Eq. 17.

Table 11. Operating conditions to validate Eq. 17

| Run	Power		Inlet		Outlet
No.	Distribution	Value	Temperature	Velocity	pressure
V1		Q	1.05*T	1.10*U	0.88*P
V2	Cosine	1.10*Q	0.90*T	0.80*U	P
V3		0.90*Q	T	1.10*U	P
V4		Q	0.95*T	1.10*U	P

Based on the calculations performed using Eq. 18, the average Re of conditions Run-V1 to V4 were approximately 5.9×10^4, 6.9×10^4, 8.6×10^4, and 9.3×10^4, respectively.

To evaluate the accuracy of Eq. 17, the calculation error and the errors of several existing and widely used correlations were compared. Previous studies[18], [21], [11] showed that the Dittus–Boelter[46], Churchill[47], Kays[48], and Pickett[49] methods are more accurate for calculating the Nu of a helium–xenon gas mixture compared with other correlations. The expressions and applicabilities of the four relationships are listed in Table 12. The accuracies of the four methods above and Eq. 17) were compared, as shown in Figure 18. Notably, the Nu values obtained from the correlations in Table 12 were calculated using the local Re, whereas used Re_{avg} was used in Eq. 17 for the calculations.
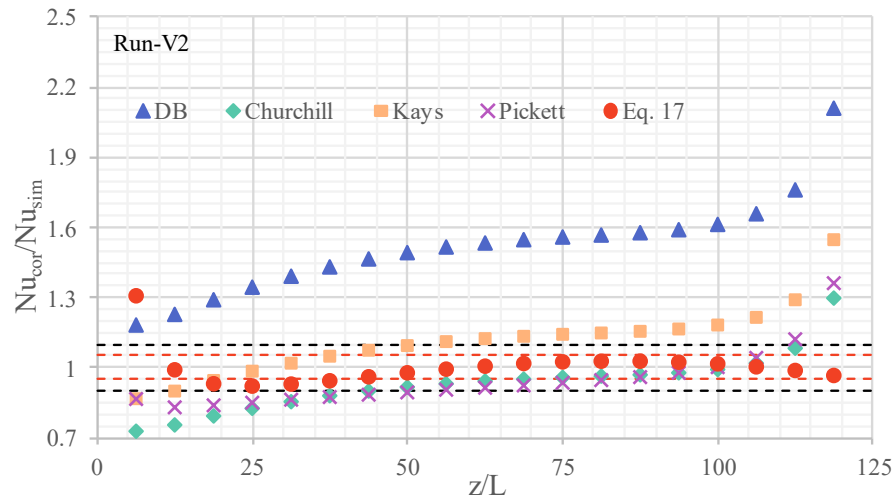
Table 12. Nut correlations

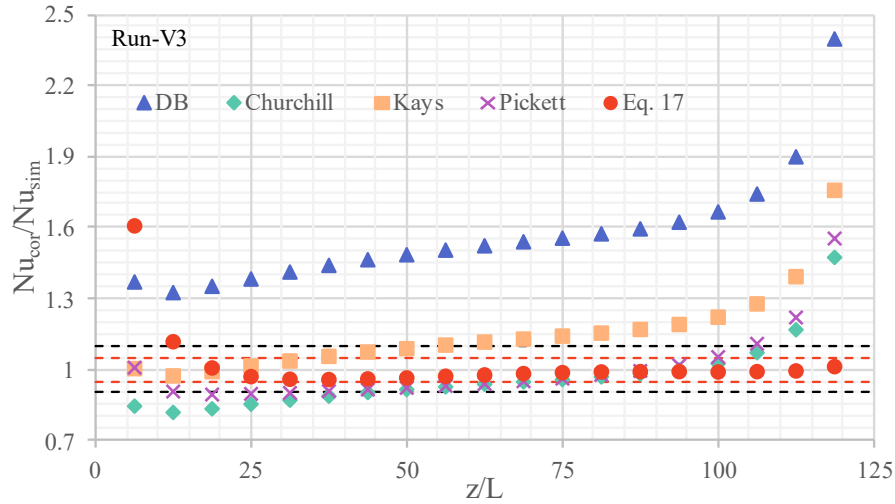| Name	Range of Re	Range of Pr	Correlations
Dittus-Boelter	Re $>10^4$	0.7<Pr<160	$Nu = 0.023Re^{0.8}Pr^{0.4}$
Churchill	Re $>10^4$	0.001<Pr < 200	$Nu = 6.3 + \dfrac{0.079Re \sqrt{f}Pr}{(1 + Pr^{0.8})^{5/6}}$ $1/\sqrt{f} = 2.21\ln(Re/7)$

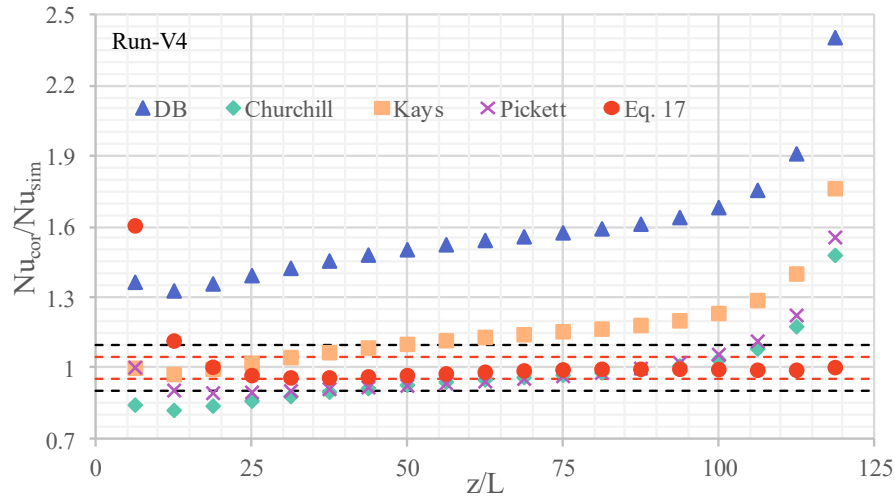| Kays | Re $>10^4$ | 0.5<Pr<1.0 | $Nu = 0.022Re^{0.8}Pr^{0.6}$ |
| Pickett | 3.12×10^4<Re<1.02 $\times10^5$ | 0.42<Pr<0.49 | $Nu = 0.021Re^{0.8}\ Pr^e\left[\left(\dfrac{t_w}{t_b}\right)^{-0.4} + \dfrac{0.85L}{z}\right]$ $e = 0.65$ |
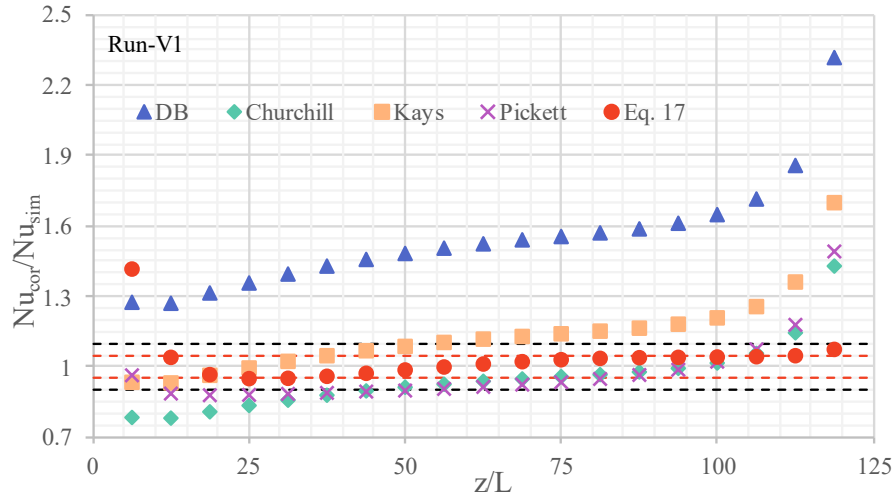
(a) Run-V1

(b) Run-V2

(c) Run-V3

(d) Run-V4

Figure 18. Comparison of calculations using different equations based on simulation results of Run-V1 to Run-V4 (relative errors within red and black dashed lines are less than 5% and 10%, respectively).

As shown in **Figure 18**, Eq. 17 demonstrated high accuracy in most axial positions, with a lower relative error compared with the Dittus–Boelter, Churchill, Kays, and Pickett correlations. Most of the observations indicated a relative error of less than 10%, except for two points near the inlet. In the latter half of the duct, almost all data points indicated a relative deviation of less than 5%. **Table 13** lists the maximum and average relative errors of each correlation for all the data points under the four operating conditions listed in **Table 11**.

Table 13. Relative error of calculation results using different correlations

		Dittus-Boelter	Churchill	Kays	Pickett	Eq. 17
Relative error	Maximin	140.2%	47.7%	76.1%	55.4%	60.6%

	Average	55.4%	11.1%	15.4%	10.3%	5.3%

As presented in **Table 13**, the Dittus–Boelter correlation showed the highest maximum and average relative errors among the five correlations, thus indicating that its predictive performance was the least ideal. However, the accuracy of Eq. 17 was the lowest, with only approximately one-half of the error indicated in the Pickett correlation, thus rendering it the most accurate among the five correlations. Furthermore, based on the calculation results for all four operating conditions, the Kays correlation yielded the most accurate prediction for the entrance area ($z/L \leqslant 18.75$), with an average relative error of 4.5%. In the outlet area ($z/L \geqslant 106.25$), Eq. 17 yielded the highest prediction accuracy, with an average relative error of 2.2%. The results above validated the theoretical derivation and confirmed the feasibility of Eq. 17 for turbulent heat transfer calculations in a helium–xenon gas mixture in a core environment.

Furthermore, Eq. 17 showed high accuracies for calculations near the outlet but exhibited low accuracy near the inlet, in contrast to other correlations. The improved accuracy of Eq. 17, particularly near the outlet, can be attributed to the inclusion of the thermal boundary layer changes caused by power fluctuations, which were not considered in the other correlations. As the power decreases rapidly near the outlet, using a correlation that disregards changes in the thermal boundary layer may result in significant distortions in the calculations. Furthermore, consistent with the observed low accuracy of the calculations near the inlet, previous studies by Sparrow et al.[34] showed similar challenges in achieving accurate calculations in this region. They attributed the cause partially to changes in the fluid properties and the uncertainty of eddy diffusivities. However, in the present study, in addition to the reasons above, the simplification of formulas in the derivation process and the viscous dissipation caused by the high-speed fluid may result in inaccurate predictions near the inlet.

The preceding discussion highlights that although Eq. 17 provides satisfactory accuracy for most axial regions in the channel, further improvements can be realized.

In this regard, the Kays correlation can be combined with Eq. 17 to derive a new segmented relationship, as shown in Eq. 21. To evaluate the effectiveness of the approach, Eq. 21 was applied to calculate the four operating conditions specified in **Table 11**, and the resulting calculation accuracy is presented in **Figure 19**.

$$Nu = \begin{cases} 0.022\, \mathrm{Re}^{0.8}\, Pr^{0.6} & (\frac{Z}{L} \leq 18.75) \\ 2\dfrac{\omega^2 + \pi^2}{\varphi\omega}\left\{\pi\left[cot(\pi z) - \dfrac{1}{sin(\pi z)\,exp(\omega z)}\right] - \omega\right\}^{-1} & (\frac{Z}{L} > 18.75) \end{cases} \qquad \text{Eq. 21}$$

$$\varphi = -90.72 \mathrm{Re}_{avg}^{-0.72} \quad \omega = 1075.65 \mathrm{Re}_{avg}^{-0.31}$$
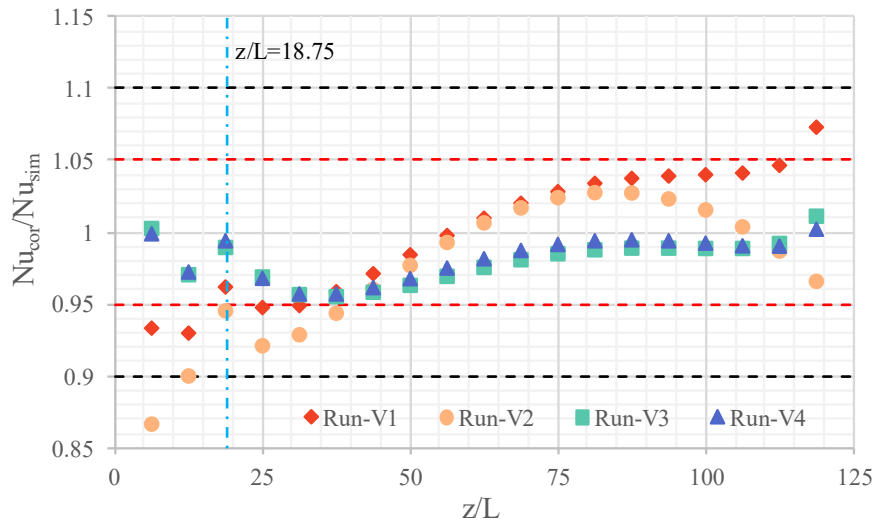

Figure 19. Comparison of Nu between simulation data and Eq. 21 (relative errors within red and black dashed lines are less than 5% and 10%, respectively)

Eq. 21 employs the Kays correlation to calculate Nu in the vicinity of the inlet (z/L ≤ 18.75). In this correlation, Re can be approximated using the principle of energy conservation. The Nu values in the remaining regions of the channel were calculated using Eq. 17. The data presented in **Figure 19** show a significant improvement in the prediction accuracy achieved via the optimized correlation (Eq. 21). Specifically, the maximum and average relative errors reduced to 13.3% and 2.9%, respectively, while a satisfactory level of accuracy was maintained throughout the channel axial range.

5. Conclusion

Numerical and theoretical investigations were conducted in this study to examine the heat transfer characteristics of a helium–xenon gas mixture in a cylindrical channel within a reactor-core environment. A multiregion conjugated heat transfer model of the channel was established, and several special operating conditions were established to analyze the effects of these factors on Nu. The correlation for the axial Nu distribution in the channel was theoretically derived by assuming a cosine distribution for the axial power. Upon confirming the unknown coefficients, the accuracy of this correlation was meticulously examined and compared with those of other correlations. The main conclusions obtained were as follows:

（1） The addition of a reflector at the inlet accelerated the axial decline rate of Nu near the inlet, whereas the addition of a reflector at the outlet presented the opposite effect, which enhanced Nu near the outlet. In the case of the cosine power distribution, the Nu near the inlet decreased significantly as the total power decreased, whereas the opposite trend was observed in the axial middle section of the channel.

（2） Heat transfer was affected by the inlet temperature, inlet velocity, and outlet pressure through their effects on the overall Re of the channel. An increase in the inlet temperature resulted in a decrease in the overall axial Nu, whereas an increase in the inlet flow velocity or outlet pressure resulted in the opposite trend. Increasing the inlet velocity reduced the axial decline rate of Nu near the inlet, whereas simultaneously increasing both the power value and inlet velocity alleviated this phenomenon.

（3） A theoretical correlation was established to calculate the axial distribution of Nu in a channel with cosine-distributed axial power. The coefficients used in the correlation were determined based on simulation data, which resulted in a semi-

empirical correlation.

（4） Within the ranges of Re and Pr simulated in this study, the obtained semi-empirical correlation demonstrated a high degree of accuracy, with an average relative error of 5.3%. Moreover, by integrating the semi-empirical correlation with the Kays correlation, the overall relative error was further reduced to 2.9%, and the calculation accuracy was satisfactory across the entire axial range of the channel.

In future studies, a comprehensive approach encompassing both experiments and simulations shall be adopted to extensively investigate the heat transfer characteristics of the helium–xenon gas mixture. This approach contributes to the verification and expansion of the methodology outlined herein. Ultimately, the newly established correlation will serve as a foundation for the development of a subchannel analysis code designed specifically for helium–xenon cooled microreactors.

Acknowledgments

References

[1] B. Zohuri, *Nuclear micro reactors*, (SPRINGER NATURE, S.l., 2021)

[2] Q. Yang, Q. Sun, X. Liu et al., Conceptual design and thermal-hydraulic analysis of a megawatt-level lead-bismuth cooling reactor for deep-sea exploration. Prog. Nucl. Energ. **145**, 104125 (2022). doi:10.1016/j.pnucene.2022.104125

[3] L.S. Mason, A comparison of Brayton and Stirling Space Nuclear Power Systems for power levels from 1 kilowatt to 10 megawatts. AIP Conf. Proc. (2001). doi:10.

1063/1.1358045

[4] S.J. Bae, J. Lee, Y. Ahn et al., Preliminary studies of compact Brayton Cycle Perfo rmance for small modular high temperature gas-cooled reactor system. Ann. Nucl. Energ. **75**, 11–19 (2015). doi:10.1016/j.anucene.2014.07.041

[5] R. Zhang, K. Guo, C. Wang et al., Thermal‑hydraulic analysis of gas‑cooled sp ace nuclear reactor power system with closed Brayton cycle. Int. J. Energ. Res. **45**, 11851–11867 (2020). doi:10.1002/er.5813

[6] C. Xu, F. Kong, D. Yu et al., Influence of non-ideal gas characteristics on working fluid properties and thermal cycle of Space Nuclear Power Generation System. E nergy. **222**, 119881 (2021). doi:10.1016/j.energy.2021.119881

[7] B. Zhou, Y. Ji, J. Sun et al., Modified turbulent prandtl number model for helium–xenon gas mixture with low Prandtl number. Nucl. Eng. Des. **366**, 110738 (2020). doi:10.1016/j.nucengdes.2020.110738

[8] J. Hilsenrath, Y.S. Touloukian, The viscosity, thermal conductivity, and Prandtl nu mber for air, O2, N2, no, H2, CO, CO2, H2O, he, and a. Int. Commun. Heat. Mas s. **76**, 967–983 (1954). doi:10.1115/1.4015029

[9] X. Chai, X. Liu, J. Xiong et al., Numerical investigation of turbulent heat transfer properties at low prandtl number. Front. Energy Res. **8**, (2020). doi:10.3389/fenrg. 2020.00112

[10] X. Cheng, N.-il Tak, Investigation on turbulent heat transfer to lead–bismuth eutec tic flows in circular tubes for nuclear applications. Nucl. Eng. Des. **236**, 385–393 (2006). doi:10.1016/j.nucengdes.2005.09.006

[11] M.F. Taylor, K.E. Bauer, D.M. McEligot, Internal forced convection to low-prandt l-number gas mixtures. Int. J. Heat Mass Transf. **31**, 13–25 (1988). doi:10.1016/0 017-9310(88)90218-9

[12] V.E. Nakoryakov, S.L. Elistratov, O.V. Vitovsky et al., Experimental investigation

of heat transfer in helium-xenon mixtures in triangle channels. J. Eng. Thermoph ys. **24**, 139–142 (2015). doi:10.1134/s1810232815020046

[13] O.V. Vitovsky, S.L. Elistratov, M.S. Makarov et al., Heat transfer in a flow of gas mixture with low Prandtl number in triangular channels. J. Eng. Thermophys. **25**, 15–23 (2016). doi:10.1134/s1810232816010021

[14] V.E. Nakoryakov, O.V. Vitovsky, Study of heat transfer of a helium–xenon mixtur e in heated channels with different cross-sectional shapes. J. Appl. Mech. Tech. Ph y. **58**, 664–669 (2017). doi:10.1134/s0021894417040101

[15] S.L. Elistratov, O.V. Vitovskii, E.Y. Slesareva, Experimental investigation of heat transfer of helium-xenon mixtures in cylindrical channels. J. Eng. Thermophys. **2 4**, 33–35 (2015). doi:10.1134/s181023281501004x

[16] O.V. Vitovsky, V.E. Nakoryakov, E.Y. Slesareva, Heat transfer of helium–xenon m ixture on the initial pipe section. J. Eng. Thermophys. **24**, 338–341 (2015). doi:10. 1134/s1810232815040062

[17] M.S. Makarov, O.V. Vitovsky, V.S. Naumkin et al., Investigation of hydraulic resi stance and heat transfer in the flow of he-xe mixture with a small Prandtl number in a quasi-triangular pipe. Int. J. Heat Mass Transf. **199**, 123427 (2022). doi:10.10 16/j.ijheatmasstransfer.2022.123427

[18] H. Qin, C. Wang, W. Tian et al., Experimental investigation on flow and heat trans fer characteristics of He-Xe Gas Mixture. Int. J. Heat Mass Transf. **192**, 122942 (2 022). doi:10.1016/j.ijheatmasstransfer.2022.122942

[19] O.V. Vitovsky, M.S. Makarov, V.E. Nakoryakov et al., Heat transfer in a small dia meter tube at high Reynolds Numbers. Int. J. Heat Mass Transf. **109**, 997–1003 (2 017). doi:10.1016/j.ijheatmasstransfer.2017.02.041

[20] V.G. Lushchik, M.S. Makarova, Heat transfer during the tube flow of an he–xe ga s mixture with a substantial pressure gradient due to the strong heating of the tube.

J. Eng. Thermophys. **95**, 1539–1547 (2022). doi:10.1007/s10891-022-02622-8

[21] B. Zhou, Y. Ji, J. Sun et al., Nusselt number correlation for turbulent heat transfer of helium–xenon gas mixtures. Nucl. Sci. Tech. **32**, (2021). doi:10.1007/s41365-021-00972-1

[22] H. Qin, S. Qiu, C. Wang, Numerical investigation on heat transfer characteristics of helium-xenon gas mixture. T. Am. Nucl. Soc. **121**, (2019). doi:10.13182/t31208

[23] D. Huang, Z. Li, L. Yu et al., Influence of helium-xenon mixing ratio on flow heat transfer characteristics of reactor channels. J. Harbin Eng. Univ. **42**, 745-750 (2021). doi: 10.11990/jheu.201909048

[24] S. Chen, H. Qin, C. Wang et al., Flow and Heat Transfer Characteristic of He-Xe Gas Mixturewith Helical Wire Structure. Atom. Energy Sci. Tech. **55**, 990-999 (2021). doi: 10.7538/yzk.2020.youxian.0479

[25] X. Shi, L. Wang, W. Chen et al., Effect of induced vortex and configuration layout on heat transfer enhancement of helium-xenon mixture. Appl. Therm. Eng. **225**, 120168 (2023). doi:10.1016/j.applthermaleng.2023.120168

[26] T. Meng, K. Cheng, F. Zhao et al., Computational flow and heat transfer design and analysis for 1/12 gas-cooled space nuclear reactor. Ann. Nucl. Energ. **135**, 106986 (2020). doi:10.1016/j.anucene.2019.106986

[27] Z. Duan, J. Zhang, Y. Wu et al., Multi-physics coupling analysis on neutronics, thermal hydraulic and mechanics characteristics of a nuclear thermal propulsion reactor. Nucl. Eng. Des. **399**, 112042 (2022). doi:10.1016/j.nucengdes.2022.112042

[28] M. Yang, Q. Sun, C. Luo et al., Development and verification of a neutronics-thermal hydraulics coupling code with unstructured meshes neutron transport model. Nucl. Tech. **46**, 78-88 (2023). doi: 10.11889/j.0253-3219.2023.hjs.46.030601

[29] Z. Han, J. Zhang, M. Wang et al., A modified system analysis code for Thermo-hydraulic calculation of hydrogen in a nuclear thermal propulsion (NTP) system. An

n. Nucl. Energ. **164**, 108632 (2021). doi:10.1016/j.anucene.2021.108632

[30] Y.-B. Liu, X.-Y. Meng, X.-S. Wang et al., Transient analysis and optimization of p assive residual heat removal heat exchanger in advanced nuclear power plant. Nuc l. Sci. Tech. **33**, 106 (2022). doi:10.1007/s41365-022-01083-1

[31] R. Lu, Z. Li, J. Zhao et al., Numerical investigation of heat transfer characteristics of high-speed and high-temperature air cooled open-cycle reactor. Appl. Therm. Eng. **179**, 115542 (2020). doi:10.1016/j.applthermaleng.2020.115542

[32] Q. Sun, H. Zhang, Numerical Study on heat transfer performance of cooling chan nels in Space Core. Appl. Therm. Eng. **210**, 118274 (2022). doi:10.1016/j.applther maleng.2022.118274

[33] A. Barletta, E. Zanchini, Laminar forced convection with sinusoidal wall heat flux distribution: Axially periodic regime. Heat Mass Transfer. **31**, 41–48 (1995). doi: 10.1007/bf02537420

[34] E.M. Sparrow, T.M. Hallman, R. Siegel, Turbulent heat transfer in the thermal ent rance region of a pipe with Uniform Heat Flux. Appl. Sci. Res. **7**, 37–52 (1957). d oi:10.1007/bf03184700

[35] R. Siegel, E.M. Sparrow, Turbulent flow in a circular tube with arbitrary internal h eat sources and wall heat transfer. J. Heat. Transf. **81**, 280–287 (1959). doi:10.111 5/1.4008203

[36] A.P. Hatton, A. Quarmby, The effect of axially varying and unsymmetrical bounda ry conditions on heat transfer with turbulent flow between parallel plates. Int. J. H eat Mass Transf. **6**, 903–914 (1963). doi:10.1016/0017-9310(63)90081-4

[37] C.-J. Hsu, Heat transfer in a round tube with sinusoidal wall heat flux distribution. AIChE J. **11**, 690–695 (1965). doi:10.1002/aic.690110423

[38] H. Shu, F. Yasunobu, Turbulent heat transfer in a tube with prescribed heat flux. I nt. J. Heat Mass Transf. **11**, 943–962 (1968). doi:10.1016/0017-9310(68)90001-x

[39] C. Guan, X. Chai, T. Zhang et al., Preliminary Lightweight Core Design Analysis of a micro‑transportable gas‑cooled thermal reactor. Int. J. Energ. Res. **46**, 17416–17428 (2022). doi:10.1002/er.8408

[40] M. Wang, Y. Wang, W. Tian et al., Recent progress of CFD applications in PWR Thermal Hydraulics Study and Future Directions. Ann. Nucl. Energ. **150**, 107836 (2021). doi:10.1016/j.anucene.2020.107836

[41] W.-T. Li, X.-K. Meng, H.-Z. Bian et al., Numerical Analysis of heat transfer enhancement on steam condensation in the presence of air outside the tube. Nucl. Sci. Tech. **33**, 100 (2022). doi:10.1007/s41365-022-01090-2

[42] W.-H. Ji, J.-J. Cheng, H.-Z. Tao et al, Numerical simulation of coupling heat transfer and thermal stress for spent fuel dry storage cask with different power distribution and tilt angles. Nucl. Sci. Tech. **34**, 26 (2023). doi:10.1007/s41365-023-01171-w

[43] W.M. Kays, Turbulent prandtl number—where are we?. J. Heat Transf. **116**, 284–295 (1994). doi:10.1115/1.2911398

[44] T. Barth, G. Lecrivain, S.T. Jayaraju et al., Particle deposition and resuspension in gas-cooled reactors—activity overview of the two European Research Projects Thins and archer. Nucl. Eng. Des. **290,** 127–134 (2015). doi:10.1016/j.nucengdes.2014.11.047

[45] C. Cheng, Z. Duan, W. Xu et al. Experimental study of the fouling deposition on heating surface of narrow rectangular channel. Nucl. Tech. **45**, 65-72 (2022). doi:10.11889/j.0253-3219.2022.hjs.45.010601

[46] F.W. Dittus, L.M.K. Boelter, Heat transfer in automobile radiators of the tubular type. Int. Commun. Heat Mass. **12**, 3–22 (1985). doi:10.1016/0735-1933(85)90003-x

[47] S.W. Churchill, Comprehensive correlating equations for heat, mass and momentu

m transfer in fully developed flow in smooth tubes. Ind. Eng. Chem. Fund. **16**, 109–116 (1977). doi:10.1021/i160061a021

[48] W.M. Kays, *Convective heat and mass transfer* (McGraw-Hill, New York, 1980)

[49] P.E. Pickett, M.F. Taylor, D.M. McEaligot, Heated turbulent flow of helium—argon mixtures in tubes. Int. J. Heat Mass Transf. **22**, 705–719 (1979). doi:10.1016/0017-9310(79)90118-2